Hybrid Model Predictive Control Framework for Efficient Operation of a Five-Port Converter Interfaced DC Microgrid

Mallick, Arghya; Mondal, Atanu; Hota, Ashish R.; Kastha, Debaprasad; Bajpai, Prabodh

DOI
10.1109/TIE.2024.3508071

Publication date
2025

Document Version
Final published version

Published in
IEEE Transactions on Industrial Electronics

Hybrid Model Predictive Control Framework for Efficient Operation of a Five-Port Converter Interfaced DC Microgrid

Arghya Mallick, *Student Member, IEEE*, Atanu Mondal, *Student Member, IEEE*, Ashish R. Hota, *Senior Member, IEEE*, Debaprasad Kastha, *Senior Member, IEEE*, and Prabodh Bajpai, *Senior Member, IEEE*

***Abstract*—In this article, a hybrid model predictive control (MPC) based novel energy management framework for a dc microgrid is proposed to efficiently manage power sharing among photovoltaic (PV) source, battery, fuel cell, and supercapacitor while meeting critical load demand and satisfying operational constraints. In particular, the proposed framework mitigates certain practical operational challenges of the fuel cell and the electrolyzer, as laid down by the manufacturers. Instead of using multiple converters, a multiport converter topology is utilized for integrating the distributed energy resources (DERs) due to fewer conversion stages, compact size, cost-effectiveness, and ease of control. For smooth operation of the multiport converter, a hierarchical control unit is developed to coordinate with the hybrid MPC based supervisory controller and proportional–integral (PI) compensator based local controllers. Finally, a 2 kW laboratory prototype of the five-port converter is integrated with real DERs. The efficacy of the proposed energy management framework is demonstrated through experimental case studies which are designed to create challenging scenarios, such as large power mismatch due to stochastic PV generation and load.**

***Index Terms*—DC microgrid, energy management, hybrid model predictive control, multiport converter.**

Received 28 February 2024; revised 23 August 2024 and 12 November 2024; accepted 15 November 2024. Date of publication 11 December 2024; date of current version 28 May 2025. This work was supported in part by the Science and Engineering Research Board (SERB), Government of India, through IMPRINT-IIC Scheme (Ref. No. IMP/2019/000451/EN), and in part by SERB sponsored Center of Excellence on Energy Aware Urban Infrastructure, IIT Kharagpur (Ref. No. IPA/2021/000081). *(Corresponding author: Arghya Mallick.)*

Arghya Mallick is with Delft Center for Systems and Control, Delft University of Technology (TU Delft), 2600 AA Delft, The Netherlands (e-mail: A.Mallick@tudelft.nl).

Atanu Mondal is with the School of Energy Science and Engineering, Indian Institute of Technology (IIT) Kharagpur, Kharagpur 721302, West Bengal, India (e-mail: atanumondal282014@kgpian.iitkgp.ac.in).

Ashish R. Hota and Debaprasad Kastha are with the Department of Electrical Engineering, Indian Institute of Technology (IIT) Kharagpur, Kharagpur 721302, West Bengal, India (e-mail: ahota@ee.iitkgp.ac.in; kastha@ee.iitkgp.ac.in).

Prabodh Bajpai is with the Sustainable Energy Engineering Department, Indian Institute of Technology (IIT) Kanpur, Kanpur 208 016, India (e-mail: pbajpai@iitk.ac.in).

Digital Object Identifier 10.1109/TIE.2024.3508071

I. Introduction

RECENT years have seen phenomenal growth in photovoltaic (PV) generation, and energy storage systems, such as battery (BESS) and fuel cells (FC). Heterogeneous operational characteristics of these entities have led to the emergence of microgrids (MGs), particularly those employing a direct current (dc) architecture, to integrate PV, BESSs, and FCs [1]. An intelligent power management strategy is essential to fully leverage the capabilities of such a hybrid mix of DERs to meet critical load demand in a reliable manner.

A significant amount of past research has focused on realizing the best possible strategy (or optimal policy) to schedule various DERs with the goal of efficiently meeting the load demand. Authors in [2] reviewed several such strategies at length. For energy management of microgrids, authors in [3] and [4] employed fuzzy control-based optimization and particle swarm optimization techniques, respectively. Authors in [5] showed experimental validation of an energy management scheme using a multiperiod gravitational search algorithm. However, none of the methods used in [3], [4], [5] guarantee the optimality of the solutions. In [6], [7], authors implemented neural network-based energy management frameworks on grid-connected microgrids. However, such methods do not necessarily meet critical operational constraints. Authors in [8], [9] applied reinforcement learning-based techniques for optimal operation of microgrids; however, real-time implementation of such methods is difficult due to high computational burden.

Compared to the above energy management strategies, model predictive control (MPC) based energy management frameworks [10], [11] have found greater acceptance among researchers due to the ability to take optimal action while satisfying operational constraints over a prediction horizon. In particular, MPC solves a multistage optimization problem in a receding horizon manner, which enables it to incorporate the latest system state information and updated forecast in each interval while computing the control action.

However, there are certain constraints of FC and electrolyzer that a conventional MPC is not equipped to handle. Manufacturers define these specific operational conditions for the FC and electrolyzer due to their peculiar constructions [12], which

TABLE I
COMPARISON OF VARIOUS METHODS WITH HYBRID MPC FOR ENERGY MANAGEMENT OF DC MICROGRIDS

Methods	Disadvantages	Advantages
Droop control [14]	Inefficient power sharing, no guarantee on constraint satisfaction, and frequent power imbalance.	Simple implementation with fast response.
Hysteresis band control [15]	Lack of optimality and robustness, no guarantee on constraint satisfaction.	Fast response.
Fuzzy logic control [3]	No guarantee of constraints satisfaction and optimality.	Provides feasible solutions.
Particle swarm optimization [4]	Lack of convergence guarantee, no guarantee of constraints satisfaction.	Possible handles nonlinear systems.
Conventional MPC [10]	Provides suboptimal solution for mixed logical dynamical systems	Guarantees on constraint satisfaction.
Hybrid MPC	Higher computational burden for larger prediction horizon.	Provides optimal solution with guaranteed constraint satisfaction.

need to be imposed to avoid device failure. Specifically, these conditions give rise to the MG operating in multiple modes, where switching from one mode to another depends on the rules defined by the manufacturers. A similar kind of challenge was addressed by authors in [13] by a rule-based MPC (RB-MPC) approach. In RB-MPC, integer variables (that represent a mode of operation) are updated outside of the optimization problem by some predefined (if-then-else) rules, which might result in suboptimal/infeasible solutions. Therefore, a hybrid MPC framework is proposed in this article to capture such mixed logical dynamical systems (where both continuous and discrete dynamics co-exist). The advantages of hybrid MPC compared to other energy management strategies are highlighted in Table I.

In the context of integrating PV generation with storage systems, multiport converters are increasingly being preferred as they offer fewer conversion stages, compact size, cost-effectiveness, and ease of control [16], [17]. Among the three main topological classifications of multiport converters (nonisolated, fully isolated, and partially isolated), the partially isolated structure stands out for its higher efficiency, greater number of ports, and superior performance in high-power applications. Since this work is intended for application in dc microgrid-based residential buildings, a partially isolated medium to high-power dc-dc five-port converter system proposed in [18] has been chosen to integrate solar PV, batteries, fuel cells, and supercapacitors into a 380 V dc bus.

There are a few studies [19], [20], [21] which presented combined experimental operation of converter interfaced multiple renewable energy sources (RESs) with advanced energy management strategies. Authors in [19], [20] used rule-based and fuzzy logic-based energy management schemes, respectively, which fail to guarantee optimal operation. Furthermore, the converter architecture employed in the dc microgrid section in [19] increased the number of power conversion stages due to the cascaded transformer structure, which leads to a reduction of overall efficiency. In [21], authors considered an MPC-based energy management strategy for microgrid operation; however, the implemented system was based on separate converters and does not include solar PV operation.

To the best of our knowledge, no prior work has reported experimental implementation of a hybrid MPC-based energy management strategy in a dc microgrid with multiport converter integrated RESs. Considering the above research gap, the novel contributions of this article are as follows.

1) A novel energy management framework based on a hierarchical control structure with a hybrid MPC-based supervisory controller and PI compensator-based local controllers is proposed.
2) The hybrid MPC is formulated for efficient power sharing among PV, battery, fuel cell, supercapacitor, and electrolyzer while incorporating user-defined rule-based operational constraints of electrolyzer operation.
3) Experimental validation of the proposed framework is carried out with an in-house developed 2 kW five-port converter and real RESs and storage systems. In order to regulate the dc bus voltage in the presence of stochastic PV generation and load, a supercapacitor is used, and an intelligent charging/discharging scheme is developed for its operation. The performance of the proposed framework is found to be superior to that of the RB-MPC framework [13] in terms of minimizing load curtailment and satisfying constraints.

II. HYBRID MODEL PREDICTIVE CONTROL FRAMEWORK

The overall schematic description of the system is shown in Fig. 1. The operation of the multiport converter is controlled by the dedicated control unit, which consists of the proposed hybrid MPC-based supervisory controller and PI compensator-based local controllers. In this section, the formulation of the supervisory controller is described.

At a given time k, the goal of the supervisory controller is to determine the input vector $u[k] = [P_{\text{bat,ch}}[k]\ P_{\text{bat,dis}}[k]\ P_{\text{fc}}[k]\ P_{\text{load,curt}}[k]\ P_{\text{pv,curt}}[k]]^\top \in \mathbb{R}^5$, where $P_{\text{bat,ch}}[k]$ and $P_{\text{bat,dis}}[k]$ represent the charging and discharging power of battery, $P_{\text{fc}}[k]$ is the operating power of fuel cell, $P_{\text{load,curt}}[k]$ denotes load curtailment and $P_{\text{pv,curt}}[k]$ denotes the curtailment in PV generation. PV curtailment is implemented by operating the PV controller in an OFF-MPPT zone. Positive values indicate power flowing into the dc bus from the DER. These inputs determine the evolution of the continuous state defined at time k as $x[k] = [\text{SoC}[k]\ \ \text{LoH}[k]]^\top \in \mathbb{R}^2$ where $\text{SoC}[k]$ denotes the state-of-charge of the battery and $\text{LoH}[k]$ denotes the level of hydrogen (LoH) of the fuel cell.

While the operation of PV, battery, fuel cell, and supercapacitor can be controlled by the proposed controller, the operation of the electrolyzer is predetermined by the manufacturer. The electrolyzer turns on when the LoH in the fuel cell reservoir is smaller than a specified lower bound LoH_{lb}, and it turns OFF when LoH exceeds a specified upper bound LoH_{ub}. Let δ_F be a binary variable with $\delta_F[k] = 1$ when the electrolyzer is on at time k, and 0 otherwise. Then, the above criteria can be stated

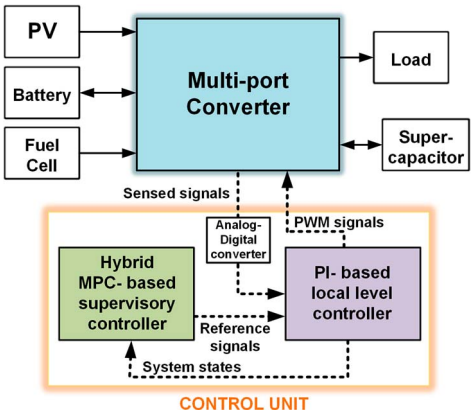

Fig. 1. Overall schematic of multiport converter operation.

formally as

$$\delta_F[k]=0 \rightarrow \delta_F[k+1]=1 \quad \text{if } \mathrm{LoH}[k] \leq \mathrm{LoH}_{\mathrm{lb}} \tag{1a}$$
$$\delta_F[k]=1 \rightarrow \delta_F[k+1]=1 \quad \text{if } \mathrm{LoH}[k] \leq \mathrm{LoH}_{\mathrm{ub}} \tag{1b}$$
$$\delta_F[k]=0 \rightarrow \delta_F[k+1]=0 \quad \text{if } \mathrm{LoH}[k] \geq \mathrm{LoH}_{\mathrm{lb}} \tag{1c}$$
$$\delta_F[k]=1 \rightarrow \delta_F[k+1]=0 \quad \text{if } \mathrm{LoH}[k] \geq \mathrm{LoH}_{\mathrm{ub}}. \tag{1d}$$

Therefore, the MG operates in one of two possible modes: one where the electrolyzer is turned on and the other when the electrolyzer is turned off. Since the operation of the electrolyzer is determined by the LoH, which is a continuous state, the resulting system belongs to the class of hybrid systems [22]. Conventional MPC techniques are not equipped for this class of systems, and thus, a hybrid MPC framework [22] is developed in this article. The dynamics of the discrete ($\delta_F[k]$) and continuous ($x[k]$) states are described next.

A. Dynamics of Electrolyzer Mode

The evolution of electrolyzer mode $\delta_F[k]$ (described above) requires the generation of two events: LoH exceeding the upper bound and reducing below the lower bound. To capture these two events, two binary variables are defined as

$$\delta_1[k]=1 \iff \mathrm{LoH}[k] \leq \mathrm{LoH}_{\mathrm{lb}} \tag{2a}$$
$$\delta_1[k]=1 \iff \mathrm{LoH}[k] \geq \mathrm{LoH}_{\mathrm{ub}}. \tag{2b}$$

The above logical relations are expressed in terms of mixed integer linear inequalities at time k as

$$\mathrm{LoH}[k]-\mathrm{LoH}_{\mathrm{lb}} \leq M_1(1-\delta_1[k]) \tag{3a}$$
$$\mathrm{LoH}[k]-\mathrm{LoH}_{\mathrm{lb}} \geq m_1\delta_1[k]+\epsilon \tag{3b}$$
$$\mathrm{LoH}[k]-\mathrm{LoH}_{\mathrm{ub}} \geq M_2(1-\delta_2[k]) \tag{3c}$$
$$\mathrm{LoH}[k]-\mathrm{LoH}_{\mathrm{ub}} \leq m_2\delta_2[k]-\epsilon \tag{3d}$$

where $M_1=(\mathrm{LoH}_{\max}-\mathrm{LoH}_{\mathrm{lb}})$, $m_1=-(\mathrm{LoH}_{\mathrm{lb}})$, $M_2=(\epsilon\mathrm{LoH}_{\mathrm{lb}}-\mathrm{LoH}_{\mathrm{ub}})$, $m_2=(\mathrm{LoH}_{\max}-\mathrm{LoH}_{\mathrm{ub}})$, $\mathrm{LoH}_{\max}$ being the maximum value of LoH and ϵ is a small positive constant. The constraints in (3a)–(3d) ensure that the binary variables $\delta_1[k]$ and $\delta_2[k]$ are assigned according to (2). The evolution of the binary variable $\delta_F[k]$ can now be stated as

$$\delta_F[k+1] \Longleftrightarrow (\delta_F[k] \wedge \sim \delta_2[k]) \vee \delta_1[k] \tag{4}$$

which is derived using the Karnaugh map (K-map) reduction technique on the truth Table II. The microgrid operator can conveniently customize such truth tables to include other types of operational characteristics of the system as well.

TABLE II
TRUTH TABLE FOR STATE TRANSITION EQUATION (1) WHERE THE SYMBOL '×' IMPLIES EITHER 0 OR 1

$\delta_F[k]$	$\delta_1[k]$	$\delta_2[k]$	$\delta_F[k+1]$
0	0	0	0
0	0	1	1
0	1	0	1
0	1	1	×
1	0	0	1
1	0	1	0
1	1	0	0
1	1	1	×

Using the techniques given in [23], [24], the above expression can be reformulated in terms of the following mixed integer linear inequalities:

$$(1-\delta_F[k+1])+\delta_1[k]+\delta_F[k] \geq 1 \tag{5a}$$
$$(1-\delta_F[k+1])+\delta_1[k]+(1-\delta_2[k]) \geq 1 \tag{5b}$$
$$\delta_F[k+1]+(1-\delta_1[k]) \geq 1 \tag{5c}$$
$$\delta_F[k+1]+\delta_2[k]+(1-\delta_F[k]) \geq 1. \tag{5d}$$

The above constraints together with (3) ensure that the binary variables evolve over time according to (1).

B. Dynamics of Battery and Fuel Cell

The dynamical model of battery as given in [10], [25] is considered here. The state-of-charge (SoC) of the battery is considered to be the state variable that evolves in discrete time as

$$\mathrm{SoC}[k+1]=\mathrm{SoC}[k]-T_sC^{-1}\left[\frac{P_{\mathrm{bat,dis}}[k]}{\eta_{\mathrm{dis}}}-P_{\mathrm{bat,ch}}[k]\eta_{ch}\right] \tag{6}$$

where C is the battery energy capacity, T_s is the sampling time of the model, $\eta_{\mathrm{ch/dis}}$ is the charging/discharging efficiency, and $P_{\mathrm{bat,ch/dis}}[k] \in \mathbb{R}_{\geq 0}$ refers to charging or discharging power of the battery at time k, respectively.

Following [26], [25], the evolution of the LoH in the fuel cell reservoir is expressed as

$$\mathrm{LoH}[k+1]=\mathrm{LoH}[k]-\frac{c_1T_s}{P_{\mathrm{fc,max}}V_{\max}}\Big[P_{\mathrm{fc}}[k]\zeta_{fc,max} - \delta_F[k]P_{\mathrm{els}}\zeta_{\mathrm{els,max}}\Big] \tag{7}$$

where P_{els} is the constant operating power of the electrolyzer. $P_{\mathrm{fc,max}}$ is the maximum operating power of the fuel cell system, $V_{\max}$ is the maximum volume of the hydrogen fuel reservoir, $\zeta_{\mathrm{fc,max}}$ and $\zeta_{\mathrm{els,max}}$ are the maximum the rates at which LoH

decreases and increases with time, and c_1 is a proportionality constant; see [25] for a more detailed discussion about the above dynamics. The electrolyzer is not shown separately in Fig. 1 as it is considered as a part of the load; whenever the electrolyzer is turned on, it draws P_{els} power from the load bus as specified by the manufacturer. Thus, the evolution of LoH depends on the discrete state δ_F.

C. Operational Constraints

While the dynamics of the discrete state and the continuous states are discussed above, the state and input variables need to satisfy several operational constraints defined below. First, power balance needs to be ensured, which is formulated as

$$\begin{aligned} &P_{\text{pv}}[k] - P_{\text{pv,curt}}[k] + P_{\text{bat,dis}}[k] + P_{\text{fc}}[k] \\ &\quad = P_{\text{load}}[k] - P_{\text{load,curt}}[k] + P_{\text{bat,ch}}[k] + \delta_F[k] P_{\text{els}}. \end{aligned} \tag{8}$$

To avoid simultaneous charging and discharging commands in (6), mixed integer constraints

$$0 \le P_{\text{bat,ch}}[k] \le P_{\text{Bat,ub}} \delta_3[k] \tag{9a}$$
$$0 \le P_{\text{bat,dis}}[k] \le P_{\text{Bat,ub}} \delta_4[k], \tag{9b}$$
$$\delta_3[k] + \delta_4[k] \le 1 \tag{9c}$$

are introduced, where $\delta_3[k]$, $\delta_4[k]$ are binary variables with at most one of them active at a given k. Finally, bounds on system states and control inputs are expressed as

$$x_{\text{lb}} \le x[k] \le x_{\text{ub}}, \tag{10a}$$
$$u_{\text{lb}} \le u[k] \le u_{\text{ub}} \tag{10b}$$

where $x_{\text{ub}}, x_{\text{lb}} \in \mathbb{R}^2$ and $u_{\text{lb}}, u_{\text{ub}} \in \mathbb{R}^5$.

D. Cost Function

The operational cost of the system at time k is defined as

$$\begin{aligned} C(u[k]) := c_{\text{bat}}(P_{\text{bat,dis}}[k] - P_{\text{bat,ch}}[k]) + c_{\text{fc}} P_{\text{fc}}[k] \\ + c_{\text{curt}}(P_{\text{load,curt}}[k] + P_{\text{pv,curt}}[k]) \end{aligned} \tag{11}$$

where the penalty factors $c_{\text{bat}}, c_{\text{fc}}$ signify the relative cost of operating the battery, fuel cell, and the cost of curtailing load. Past works, such as [27, Table 7], have estimated that the normalized cost of operating a battery is smaller than that of a fuel cell. In addition, since satisfying load demand is the primary objective of a microgrid together with renewable energy integration, we have chosen a larger penalty for curtailment by setting $c_{\text{bat}} < c_{\text{fc}} < c_{\text{curt}}$. The function $C(u[k])$ can be compactly stated as $c^\top u[k]$, and the cumulative cost over a prediction horizon length of N_p is stated as

$$J(u[k], u[k+1], \ldots, u[k+N_p-1]) = \sum_{i=k}^{k+N_p-1} c^\top u[i]. \tag{12}$$

E. Multistage Optimization Problem

The hybrid MPC controller solves the following multistage optimization problem to minimize the cumulative cost defined above subject to hybrid dynamics and operational constraints

$$\min_{\substack{\{u[k], x[k+1], \\ z[k]\}_{k\in[N_p]}}} J(u[k], u[k+1] \ldots u[k+N_p-1]) \tag{13a}$$
$$\text{s.t. } H_x x[k+1] + H_u u[k] + H_z z[k] \le h \tag{13b}$$
$$G_x x[k+1] + G_u u[k] + G_z z[k] = 0 \tag{13c}$$

where the constraints hold for $k \in \{1, 2, \ldots, N_p\}$, $z[k] = [\delta_F[k] \;\; \delta_1[k] \;\; \delta_2[k] \;\; \delta_3[k] \;\; \delta_4[k]]^\top$ is the vector of binary variables, and $H_x, H_u, H_z, G_x, G_u, G_z$ are matrices and h is a vector of suitable dimensions. Note that (13b) is a compact representation of constraints associated with discrete state (electrolyzer mode) dynamics (3), (5), mixed integer constraints of battery in (9), and the bounds on systems states and inputs in (10). Similarly, (13c) encodes continuous state dynamics (6), (7) and power balance (8). The above problem is an instance of a mixed-integer linear program.

It is assumed that load ($P_{\text{load}}[k]$) and PV generation ($P_{\text{pv}}[k]$) forecast are available to the controller over the prediction horizon which is required for the power balance constraint. The above optimization problem is solved in a receding horizon fashion, i.e., the problem is solved at each sampling time, only the first input is applied to the system, the states are allowed to evolve, and the problem is again solved at the next sampling time with the current measured value of the state variables as input to the problem. Repeatedly solving the problem improves robustness against model uncertainty as well as PV and load forecast error. The proposed hybrid MPC includes both continuous as well as discrete decision-variables, and hence it is a combination of continuous control set (CCS) and finite control set (FCS) MPC frameworks.

III. Integration With Multiport Converter

The supervisory control framework proposed in Section II works in closed-loop with the local level controller as shown in Fig. 1, which in turn generates pulse width modulation (PWM) signals for the multiport converter, which interfaces with the DERs and storage systems. The topology of the multiport converter and its (local) control are now presented.

1) Multiport Converter Topology: Fig. 2(a) shows the circuit diagram of a five-port dc–dc converter, as introduced in [18]. This converter comprises of four distinct subconverters, specifically subconverters 1, 2, 3, and 4, along with three high-frequency three-winding transformers (HFT). Port-1 is designated for the connection of a battery bank, while port-3 is intended for integrating a fuel cell stack. Port-5 serves as a direct connection point for solar PV, linking it to the series configuration of subconverter 1 and subconverter 3. As a result, photovoltaic (PV) power has the capability to be directed to the load terminal (i.e., port-2) via the same converters utilized by the battery and the fuel cell. The power handled by each converter is determined by their respective dc link capacitor voltages (v_1 and v_3). Additionally, a portion of the PV power

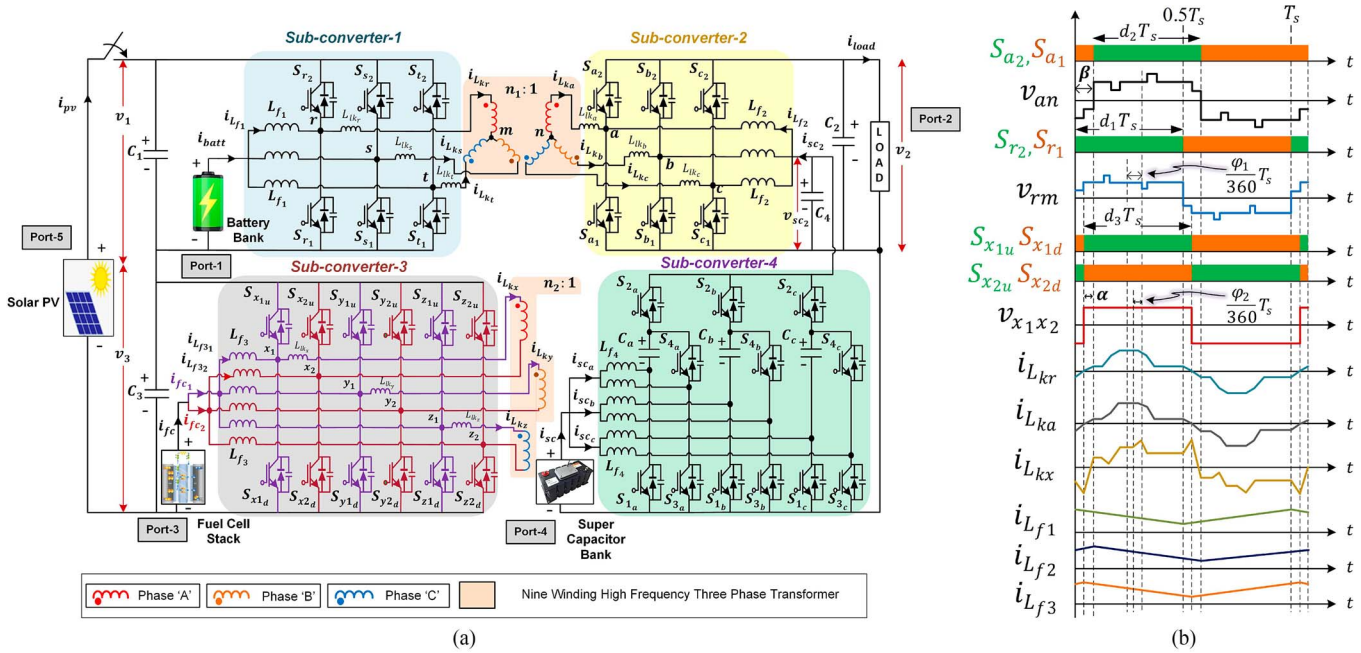

Fig. 2. (a) Circuit diagram of the five-port dc–dc converter. (b) Its key operating waveforms.

can be channeled to charge the battery bank through subconverter 1. With the exception of port-3 and port-5, all ports support bidirectional operation.

Subconverter 2 enables two-stage integration of the low voltage supercapacitor bank at port-4 with common ground to the load terminal via subconverter 4 to ensure tight regulation of the load bus voltage. In addition, the switch node points on each leg of subconverter 2 create a high-frequency ac link to connect the windings of every single phase three winding HFT. Thus, this converter channels the power flowing from PV, battery, fuel cell, and supercapacitor to the load terminal.

It is to be noted that this converter structure is proposed for medium to high power applications where each source can deliver up to 10 kW power. Fuel cells up to 10 kW typically operate below 70 V [28], while higher capacitance supercapacitor modules operate below 60 V [29]. To supply 10 kW power, these sources will be required to supply a current close to 200 A. Therefore, a multiphase structure is necessary. In particular, the six-leg structure for subconverters 3 and 4 reduces the current stress on the switches, filter inductors, and transformer windings below 50 A. Moreover, to reduce ripple current flowing through the sources, each port has a multiphase interleaved boost structure. Six interleaved phases of subconverter 3 naturally make provision for the connection of one set of three windings of a three-phase HFT, which are magnetically coupled to two other sets of three-phase windings supplied by subconverters 1 and 2. As the input voltages of these two sub-converters are considerably high, three-leg interleaved structures are sufficient for them. This causes an increase in the number of switches in the selected topology. However, due to the use of multiwinding HFT, the selected five-port dc-dc converter still uses a smaller number of switches, gate driver circuits, and magnetic cores compared to the separate converter structure based three-phase DAB [30], [31] as shown in Table III.

TABLE III
COMPARISON OF NUMBER OF COMPONENTS REQUIRED FOR THE SEPARATE CONVERTER BASED STRUCTURE AND THE SELECTED FIVE-PORT CONVERTER

Topology	No. of Transformer Core	No. of Inductor Core	No. of Switches
Separate converter structure based three-phase DAB [30], [31]	12	18	60
Selected five-port converter [18]	3	18	36

Fig. 2(b) displays a representative set of waveforms for the voltages across and current through the transformer windings as well as filter inductor currents. The current through the filter inductor of one leg of each subconverter (specifically, subconverters 1, 2, and 3) is depicted for simplicity. These waveforms are obtained for a fixed value of phase shift angles (ϕ_1 and ϕ_2) and a duty ratio of 50%. In this context, the notations d_1, d_2, and d_3 denote the duty ratios associated with the top switches of subconverters 1, 2, and 3, respectively, while d_4 denotes the duty ratio of the bottom switches of subconverter 4. The phase shift angles ϕ_1 and ϕ_2 play a pivotal role in determining the distribution of power through the HFT among subconverters 1, 2, and 3. This calculation is based on taking the phase voltage (v_{an}) of the winding on the subconverter 2 side as the reference waveform. The convention used here considers ϕ_1 and ϕ_2 as positive when v_{rm} leads v_{an} and when $v_{x_1x_2}$ leads v_{an}, respectively. Reference [18] provides an in-depth description of the operational principles and theoretical analysis of this converter for application towards hybrid energy sources and storage systems. Subconverter 4 is described in details in reference [32].

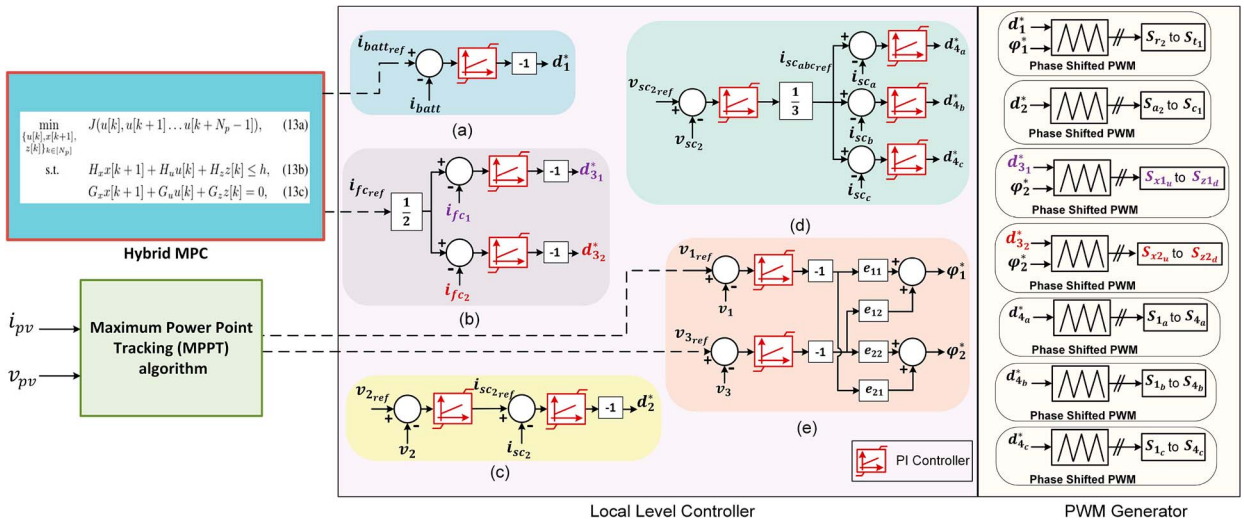

Fig. 3. Master–slave control schematic with focus on the local level control diagram of five-port dc–dc converter. (a), (b) Current controllers of subconverter 1 and 3. (c), (d) Nested loop structures of subconverters 2 and 4. (e) Decoupled phase shift controller. The dashed lines indicate the signals that flow to the local controller from the hybrid MPC and MPPT algorithms.

2) Local Level Controller: It is desired that the multiport converter operates by effectively and seamlessly allocating power among various energy sources and energy storage devices while maintaining precise control of the converter bus voltages. In this context, Fig. 3 shows an overview of the control structure for the five-port dc-dc converter. It employs a nested loop structure consisting of outer voltage loops and inner current loops for both subconverters 2 and 4, as depicted in Fig. 3(c) and 3(d). These control loops are instrumental in tightly regulating the load bus voltage (v_2) and the output terminal voltage (v_4) of subconverter 4.

The current loops are illustrated in Fig. 3(a) and 3(b), and are responsible for tracking the current commands [provided by converting the optimal input found by solving (13) into reference current values] for the battery and fuel cell, generating appropriate duty ratio commands, and subsequently producing PWM pulses for the insulated gate bipolar transistor (IGBT) switches of their respective subconverters. Since subconverters 1, 2, 3, and the HFT together constitute a three phase triple active bridge [33] (TP-TAB), a decoupled phase shift controller [Fig. 3(e)] is employed which generates the necessary phase shift angle commands to facilitate smooth power flow through the high-frequency transformer while also regulating the bus voltages v_1 and v_3 to the reference values which are generated from the maximum power point tracking algorithm. In this context, the variables e_{11}, e_{12}, e_{21}, and e_{22} represent the elements of the decoupling matrix [33].

3) Role of Supercapacitor in Balancing Power Mismatch: The supercapacitor bank is utilized as a slack source to compensate for power imbalance, which occurs due to the difference between actual PV generation/load and forecast. The cascade configuration of subconverters 2 and 4 necessitates the deviation in dc bus voltage ($v_{\mathrm{sc},2} = v_4$) of subconverter 4 during power imbalance in load bus voltage (v_2). The controller of subconverter 4 takes the difference of v_4 from its nominal value (190 V) as input and provides the necessary charging/discharging current command to the supercapacitor. Further, it is necessary to keep the voltage of the supercapacitor (input voltage of subconverter 4, denoted by v_{sc}) within permissible upper bound (V_{ub}) and lower bound (V_{lb}). It is proposed that if v_{sc} hits V_{lb} (or V_{ub}), the supercapacitor is charged (discharged) at a constant rate P_{sc} till the voltage hits $0.5(V_{\mathrm{lb}} + V_{\mathrm{ub}})$. Thus, an artificial load demand (P_{sc}) is added/removed from the system to charge/discharge the supercapacitor when v_{sc} hits the bounds.

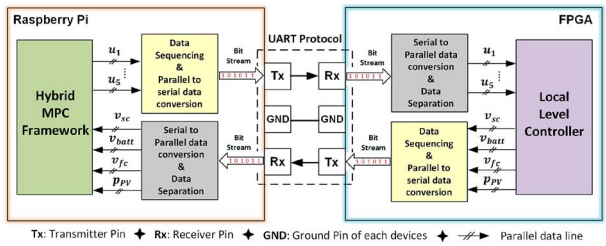

Fig. 4. Communication between Raspberry Pi and FPGA.

4) Communication Between Supervisory and Local Level Controller: Fig. 4 illustrates the bi-directional communication between the supervisory and local level controller via universal asynchronous receiver/transmitter (UART) communication protocol. After the conversion of data types, the serial data is encrypted by adding suitable buffers in its sequence and sent to the TX terminal. Data separation takes place following the decryption of the received data at the RX terminal. In each interval, the updated data from both controllers are exchanged in redundancy so that the decryption algorithm can identify inconsistencies between two consecutive series of identical data chains. In addition to using shielding wires, this security patch shields the data from getting corrupted by external noises such as electromagnetic interference (EMI).

5) Practical Implementation Challenges: To maintain a smooth operation of the converter-based dc microgrid, it is important to consider the following practical challenges.

a) *Computational Requirements:* The optimization problem in (13) is a mixed integer linear program, which is solved in

an embedded controller. Since the total number of decision variables is smaller than 100, the problem can be solved within a minute by an industry-standard solver. Typically, (13) is supposed to be solved repeatedly every 15 min, which is an adequate duration for the computation to take place.

b) *Sensor Accuracy:* The signals sensed from different current and voltage sensors of the power converter decide the system states, which are fed back to the hybrid MPC. Any error in the system states due to the inaccuracy of sensors might result in a power imbalance in the dc bus. However, the supercapacitor can tackle such minor power imbalances efficiently to maintain safe and reliable operation of the dc microgrid.

c) *Delay Compensation:* The hybrid MPC implemented on the embedded controller communicates with an FPGA-based local level controller through serial UART communication protocol where the typical delays are in the order of milliseconds to a few seconds [34]. To reduce the impact of delays, one could adopt compensation techniques such as step-ahead prediction while formulating the MPC problem. In the worst case, there could be a sustained power imbalance in the dc bus due to delayed communications for a few hundred milliseconds, which can be comfortably handled by the supercapacitor.

d) *Model Uncertainties:* One of the key strengths of hybrid MPC is to repeatedly update the problem in (13) with the latest system state information. Such policy inherently induces robustness against model uncertainties. However, one could use nonlinear MPC in case there is a significant error in the linearized model.

Remark 1: The hybrid MPC framework developed in Section II has no dependence on the topology of the multiport converters. The problem in (13) is solved in an embedded controller, which propagates control inputs to the local level controllers. All these local-level controllers can be designed in various ways with appropriate adjustments for a specific topology of the converters. For instance, the power-sharing strategy among the ports in Fig. 3 is embedded in the structure of the local level controller, which might change with the topology of the converter without changing the hybrid MPC formulation. On the other hand, increasing/decreasing the number of energy storage systems will respectively add/remove additional constraints [similar to (6) or, (7)] and penalty terms in the objective function of (13). In addition, one can also consider a hybrid ac–dc microgrid by adding an inverter-integrated ac load to port 2 of Fig. 2(a). In that case, P_{load} in (8) needs to be updated as the combination of dc and ac load.

IV. Results and Discussion

This section illustrates the effectiveness of the proposed framework via numerical and experimental case studies.

A. Numerical Simulation Results

The proposed hybrid MPC-based framework is compared with a rule-based MPC [13] (RB-MPC) scheme to show that the proposed framework is better suited to deal with the user-defined operation of the electrolyzer. The multistage optimization problem in (13) is modeled using Pyomo and solved by the MOSEK solver. The prediction horizon (N_{p}) and the values of relevant parameters related to problem (13) are given in Table IV. Note that a large value of N_{p} increases the computational burden, whereas a small N_{p} results in poor performance. Therefore, a judicious value of N_{p} should be chosen by the designer depending on the compute platform devoted to solve the optimization problem (13). The computation time is of the order of a few seconds. As a result, a small sampling time can be chosen, which will be beneficial in tackling uncertainty in PV generation and load.

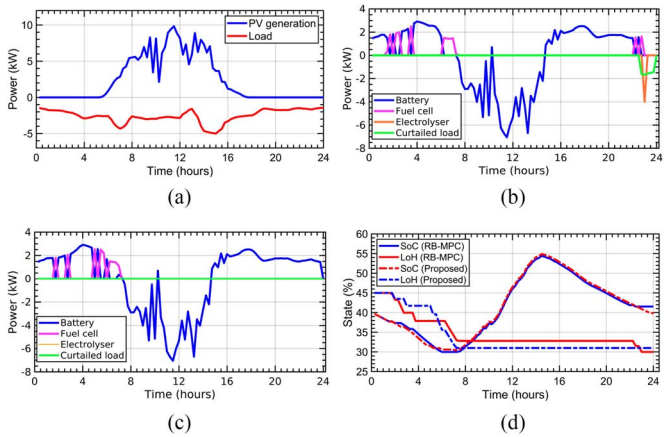

Fig. 5. (a) 24-h long past data of real PV generation and load. (b) Solution profiles of system components under RB-MPC [13] method. (c) Solution profiles under the proposed hybrid MPC. (d) Profiles of states of the storage elements (battery and fuel cell) under both methods.

In this case study, the dc microgrid is simulated with real PV generation and load data, as shown in Fig. 4(a). Under RB-MPC, the battery and fuel cell fails to meet the load demand between $23-24$ h, as shown in Fig. 4(b). Fig. 4(d) shows that the FC reservoir quickly runs out of stored energy as the LoH hits the lower bound of 30%, which leads to the turning on of the electrolyzer operation. The battery alone can not supply the required energy for the load and electrolyzer operation throughout the horizon N_{p} due to its low SoC level. To maintain the feasibility of the RB-MPC based solution, 2.54% of total load (here, total load implies the aggregated load of 24 h) had to be curtailed during $23-24$ h. as shown in Fig. 4(b). Furthermore, the operation of the electrolyzer ceases for the same reason. Under the proposed hybrid MPC framework, FC does not operate between $23-24$ h as shown in Fig. 4(c), which results in LoH $> 30\%$. The electrolyzer remains turned off. As a result, no load curtailment is required in the hybrid MPC solution as the battery continues to supply the load during $23-24$ hrs.

The difference in the results is because RB-MPC does not anticipate that the electrolyzer is going to turn on within the prediction horizon if the fuel cell is used. RB-MPC formulation does not consider the evolution of the discrete modes of operation. In contrast, the proposed hybrid MPC framework

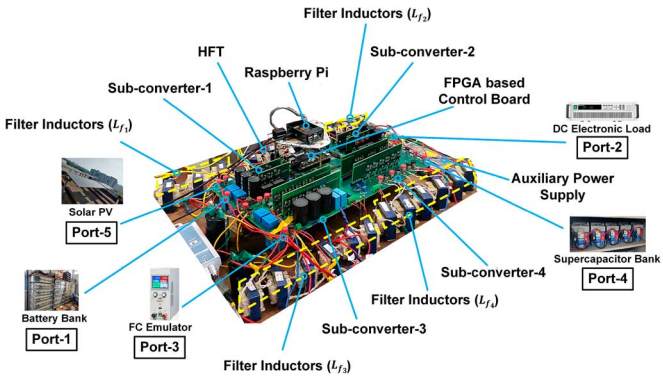

Fig. 6. Experimental setup of five-port dc–dc converter.

TABLE IV
PARAMETER VALUES USED IN EXPERIMENTAL STUDY

Parameter	Value	Parameter	Value
N_p	10	v_2	380 V
v_{bat}	200−240 V	L_{f_4}	704 μH
v_{fc}	43−54 V	PV voltage	485−560 V
v_{sc}	36−56 V	v_1	398−460 V
C_1, C_2, C_4	676 μF	L_{f_1}, L_{f_2}	3 mH
v_3	86−100 V	L_{f_3}	380 μH
C_3	3016 μF	C_a, C_b, C_c	117 μF
v_{sc2}	190 V	c_{bat}	1
c_{fc}	1.5	c_{curt}	5

considers the implications of turning on the electrolyzer which may lead to serious load curtailment if done at an improper time of the day, and avoids using the fuel cell.

B. Experimental Validation

An experimental prototype of a 2 kW five-port converter has been developed to validate the proposed energy management framework. The prototype is shown in Fig. 6. The subconverters 1 and 2 use IKW40N120T2FKSA1 IGBT switches, and subconverters 3 and 4 use IKW20N65ET7XKSA1 IGBT switches from Infineon Technology. The subconverters 1, 3, and 4 are rated for 1 kW power, and subconverter 2 is designed to process maximum 2 kW power. The operating switching frequency of the system is 20 kHz.

In this design, the nine-winding HFT is realized by three single-phase three-winding HFTs. Every single phase three-winding HFT is designed by using EE 65/32/27 Ferrite core having a number of turns 38, 33, and 17 corresponding to winding 1, 2, and 3 respectively (where winding 1, 2, and 3 denotes the transformer winding of each single phase three-winding transformer connected to subconverter 1, 2, and 3 respectively). The litz wire of 38 SWG 50 strands is used for windings 1 and 2, whereas winding 3 uses 38 SWG 100 strands litz wire. The kVA ratings of respective windings are 0.613, 0.905, and 0.642 kVA. The design of these three-winding HFT is done according to the standard design procedure given in [35].

The control unit uses AMD Artix 7 FPGA (XC7A50T-1FGG484C) as the local level controller and Raspberry Pi 4B

TABLE V
SPECIFICATIONS OF THE ENERGY STORAGE ELEMENTS

Storage	Specifications
Battery	5 kWh/220 V
Fuel cell (emulator)	1.2 kW/48 V
Supercapacitor	650 F/36 Wh/(36−56) V

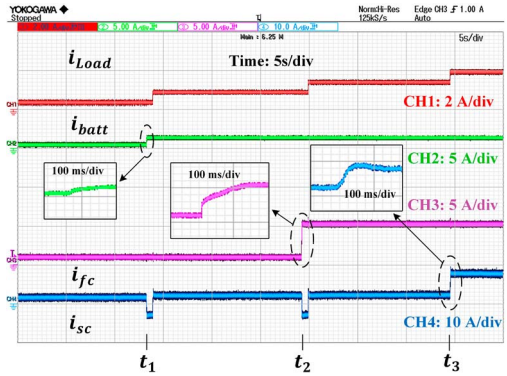

Fig. 7. Response of battery, fuel cell, and supercapacitor current for a step change in load current.

micro-controller as the supervisory controller (Fig. 1). In addition, two MAX1304ECM 8-channel ADC from Analog Devices are employed to convert various sensor data into digital signals. The values of different system parameters are given in Table IV. Similar to design procedure mentioned in [36], the filter capacitance (C_1, C_2, C_3, and C_4) and series capacitance (C_a, C_b, and C_c) of subconverter 4 are selected by considering $< 1\%$ ripple voltage of the respective rated values. Whereas, filter inductors L_{f_1}, L_{f_2} are chosen based on $< 15\%$ ripple current and L_{f_3}, L_{f_4} are designed by considering $< 2\%$ ripple current of the respective rated values. This ensures the proper suppression of ripple voltage across the dc link capacitors as well as a reduction in the ripple currents of different current-fed ports (ports 1, 3, and 4). It is to be noted that to avoid excessive filter inductance value due to the higher voltage and lower current rating, the percentage ripple current is deliberately chosen higher at port 1 ($< 15\%$) compared to port 3 and 4 ($< 2\%$).

As depicted in Fig. 6, port 1 connects to an HBL VRLA battery bank. At port 4, a 650F, 56 V supercapacitor bank is provided. Port 5 is connected to an array of 12 STION 140 Wp solar panels arranged in series. For dc loading, an IT8800 Programmable dc electronic load is used at port 2. Port 3 is equipped with an EPS-9200-25T programmable unidirectional power supply to emulate a fuel cell stack. Table V presents the specifications of the energy storage elements used in this work. In general, fuel cells possess higher energy density compared to batteries and supercapacitors but lack power density. On the other hand, the supercapacitor is superior in terms of power density, but shows poor energy density. This comparison is often depicted via a Ragone plot; see [37] for a detailed discussion. Therefore, unlike batteries and fuel cells, supercapacitors are suitable to handle high amounts of power for a shorter period of time. Four case studies are presented below to evaluate the performance of the proposed framework.

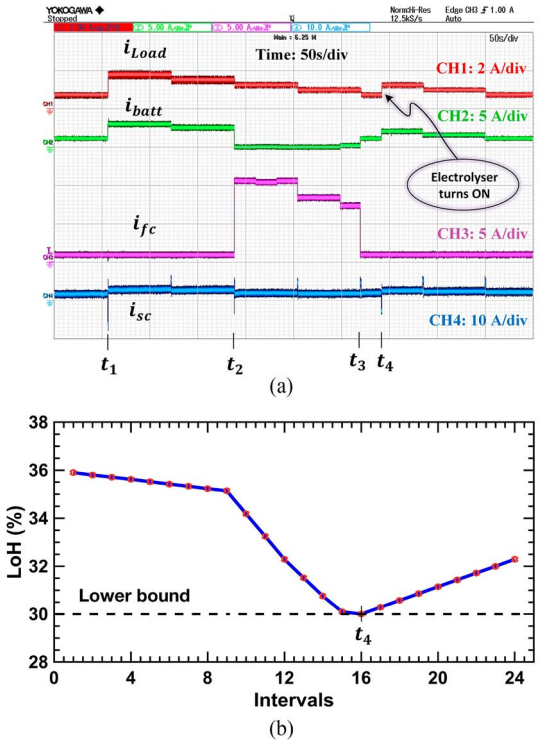

Fig. 8. (a) Preemptive power delivery by fuel cell. (b) LoH profile of fuel cell computed using (7).

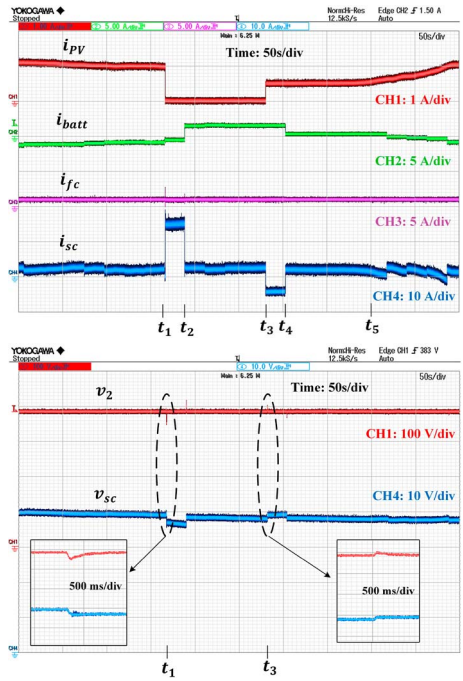

Fig. 9. Current profiles of PV, battery, fuel cell and supercapacitor (top), voltage profiles of load bus and supercapacitor port (bottom). As the supercapacitor suddenly discharges, the dc bus voltage sees a sharp undershoot. A similar overshoot of dc bus voltage occurs at the start of supercapacitor charging.

1) Tracking and Transient Responses of Subconverters: In order to analyze the transient behavior of the battery current, fuel cell current, and supercapacitor current, the system is subjected to a step load change of 200 watts at time instances t_1, t_2, and t_3, as depicted in Fig. 7. Additionally, at t_1 and t_2, the reference current for the battery and fuel cell are also changed to maintain power balance. It is to be noted that these reference current signals are given just to test each converter's response and are not a solution of (13). It is observed that the transition of the battery current in response to the change in the reference value is smooth and swift, settling within 20 ms. In contrast, the fuel cell current loop is deliberately designed to respond slowly, with a settling time of 60 ms, to mimic the sluggish response characteristics of the fuel cell stack. Given that subconverters 2 and 4 operate within a nested loop control structure, the supercapacitor reacts quickly enough (with settling time 50 ms) to regulate the load bus voltage (v_2). It is worth mentioning that there is an unavoidable delay in load changes, resulting in a brief period during the transitions at t_1 and t_2 where the supercapacitor current briefly goes negative to maintain power balance.

2) Preemptive Operation of Fuel Cell : In this study, the transition between fuel cell and electrolyzer operation is demonstrated with intelligent preemptive power delivery by the fuel cell. In Fig. 8(a), a ramping down load reference is given to the system at t_1. The battery alone is capable of serving the load from t_1, however, the fuel cell also delivers power between t_2 and t_3 to drive the initial LoH level (i.e. 36%) down to LoH_{lb} (i.e., 30%) as shown in Fig. 8(b). As the initial LoH level is very close to the lower bound, it is expected to hit LoH_{lb} soon. However, the look ahead nature of hybrid MPC helps to realize that turning on the electrolyzer will not result in infeasible solution, rather it is a good opportunity as the load profile is ramping down in near future. Such a preemptive power delivery showcases the positive impact of having a large prediction horizon (N_p), which allows the system to adapt and benefit from the continuously varying future load profile. At t_4, the LoH level hits the lower bound, and the electrolyzer turns on according to the user-defined criteria explained in Section II. With the turning on of the electrolyzer, the net load of the system increases by 200 W from t_4, which gets supplied by the battery. From t_4, the LoH level gradually increases, as shown in Fig. 8(b). Thus the proposed framework ensures the timely operation of the electrolyzer without disturbing the power balance.

3) Tackling Uncertainty of PV Generation: In this study, the efficacy of the supercapacitor tackling uncertainty in PV generation is demonstrated in Fig. 9 for a constant load of 400 Watts. At t_1, the PV power is suddenly reduced to zero to emulate sudden weather changes to cause a large error in the PV forecast. The hybrid MPC solver is not aware of this information until the next sampling interval at t_2. Therefore, the supercapacitor starts providing the required power to mitigate power imbalance and regulates the dc bus voltage around the rated value. The dip in the dc bus voltage at t_1 is observed to be -7.21% of the rated value. At t_2, the measured PV power is updated to zero, and the optimization problem at (13) recomputes the solution, which restores the power balance in the MPC

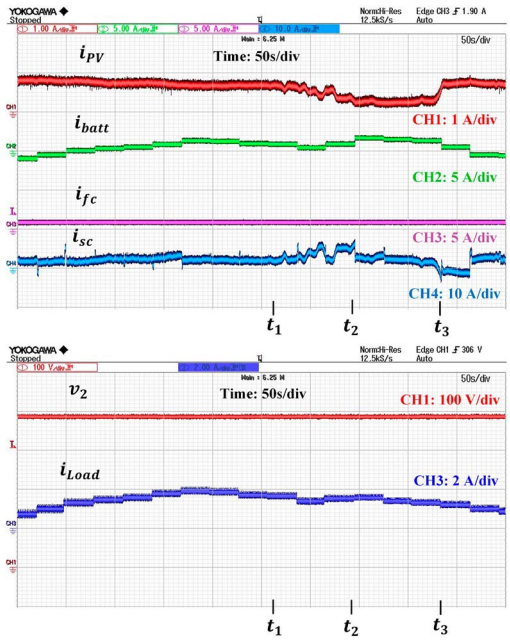

Fig. 10. Current profiles of PV, battery, fuel cell, and supercapacitor bank (top), load bus voltage and load current profile (bottom).

solution. Thus, it is no longer necessary for the supercapacitor to provide any power to the dc bus. A similar incident takes place at t_3 when PV power suddenly jumps from zero, which was not anticipated by the hybrid MPC. Consequently, the supercapacitor rescues the system from probable power imbalance by absorbing additional PV generation. The overshoot in the dc bus voltage at t_3 is $+5.26\%$ of the rated value. In addition to such discrete jumps, smooth variation in PV generation is also handled by the supercapacitor, as seen after t_5 in Fig. 9. Thus, the key role of the supercapacitor in maintaining dc bus voltage despite uncertainty in PV generation is illustrated.

4) Tackling Natural Intermittency in PV Generation and Varying Load Demand: In this study, a realistic scenario of dc microgrid operation is considered where intermittent PV and varying load demand interact with different energy storage systems. In Fig.10, PV delivers power with significant natural intermittency between t_1 and t_3 while the load power is variable throughout the operation. The battery, supercapacitor, and fuel cell jointly manage the power balance of the microgrid and smoothly handle the natural intermittency of the RESs. In particular, the natural variation of PV power between t_1 and t_2 is adjusted by the proportionate actions of the supercapacitor, and the sustained low generation of PV during t_2 and t_3 is adequately compensated by increased power delivery of the battery. Finally, the well-regulated profile of load bus voltage (v_2) in Fig. 10 (bottom) throughout the operation confirms the power balance in the system showcasing a testament to the robustness of the proposed framework.

V. Conclusion

In this article, a hybrid MPC-based energy management framework is proposed for a dc microgrid consisting of solar PV generation, battery, supercapacitor, fuel cell, and electrolyzer to mitigate the rule-based operational challenges of the electrolyzer. A dedicated control unit based on the proposed framework has also been developed for the smooth operation of a five-port converter that integrates the above DERs. Simulation results showed the superiority of the hybrid MPC over RB-MPC methodology in handling complex rule-based operations. Experimental results verified the feasibility of the power-sharing scheme computed by the hybrid MPC scheme, and the effectiveness of the supercapacitor in regulating the dc bus voltage.

References

[1] D. L. Gerber, V. Vossos, W. Feng, C. Marnay, B. Nordman, and R. Brown, "A simulation-based efficiency comparison of AC and DC power distribution networks in commercial buildings," *Appl. Energy*, vol. 210, pp. 1167–1187, 2018.

[2] M. F. Zia, E. Elbouchikhi, and M. Benbouzid, "Microgrids energy management systems: A critical review on methods, solutions, and prospects," *Appl. Energy*, vol. 222, pp. 1033–1055, 2018.

[3] Y.-K. Chen, Y.-C. Wu, C.-C. Song, and Y.-S. Chen, "Design and implementation of energy management system with fuzzy control for DC microgrid systems," *IEEE Trans. Power Electronics*, vol. 28, no. 4, pp. 1563–1570, Apr. 2013.

[4] M. Manbachi and M. Ordonez, "AMI-based energy management for islanded AC/DC microgrids utilizing energy conservation and optimization," *IEEE Trans. Smart Grid*, vol. 10, no. 1, pp. 293–304, Jan. 2019.

[5] M. Marzband, M. Ghadimi, A. Sumper, and J. L. Domínguez-García, "Experimental validation of a real-time energy management system using multi-period gravitational search algorithm for microgrids in islanded mode," *Appl. Energy*, vol. 128, pp. 164–174, 2014.

[6] T. Wang, X. He, and T. Deng, "Neural networks for power management optimal strategy in hybrid microgrid," *Neural Comput. Appl.*, vol. 31, pp. 2635–2647, 2019.

[7] M. E. G. Urias, E. N. Sanchez, and L. J. Ricalde, "Electrical microgrid optimization via a new recurrent neural network," *IEEE Syst. J.*, vol. 9, no. 3, pp. 945–953, Sep. 2015.

[8] G. K. Venayagamoorthy, R. K. Sharma, P. K. Gautam, and A. Ahmadi, "Dynamic energy management system for a smart microgrid," *IEEE Trans. Neural Netw. Learn. Syst.*, vol. 27, no. 8, pp. 1643–1656, Aug. 2016.

[9] E. Kuznetsova, Y.-F. Li, C. Ruiz, E. Zio, G. Ault, and K. Bell, "Reinforcement learning for microgrid energy management," *Energy*, vol. 59, pp. 133–146, 2013.

[10] A. Parisio, E. Rikos, and L. Glielmo, "A model predictive control approach to microgrid operation optimization," *IEEE Trans. Control Syst. Technol.*, vol. 22, no. 5, pp. 1813–1827, Sep. 2014.

[11] J. P. Torreglosa, P. García, L. M. Fernández, and F. Jurado, "Predictive control for the energy management of a fuel-cell–battery–supercapacitor tramway," *IEEE Trans. Ind. Inform.*, vol. 10, no. 1, pp. 276–285, Feb. 2014.

[12] L. Valverde, C. Bordons, and F. Rosa, "Integration of fuel cell technologies in renewable-energy-based microgrids optimizing operational costs and durability," *IEEE Trans. Ind. Electron.*, vol. 63, no. 1, pp. 167–177, Jan. 2016.

[13] T. Pippia, J. Sijs, and B. De Schutter, "A single-level rule-based model predictive control approach for energy management of grid-connected microgrids," *IEEE Trans. Control Syst. Technol.*, vol. 28, no. 6, pp. 2364–2376, Nov. 2020.

[14] U. B. Tayab, M. A. B. Roslan, L. J. Hwai, and M. Kashif, "A review of droop control techniques for microgrid," *Renewable Sustain. Energy Rev.*, vol. 76, pp. 717–727, 2017.

[15] D. Ipsakis, S. Voutetakis, P. Seferlis, F. Stergiopoulos, S. Papadopoulou, and C. Elmasides, "The effect of the hysteresis band on power management strategies in a stand-alone power system," *Energy*, vol. 33, no. 10, pp. 1537–1550, 2008.

[16] A. K. Bhattacharjee, N. Kutkut, and I. Batarseh, "Review of multiport converters for solar and energy storage integration," *IEEE Trans. Power Electron.*, vol. 34, no. 2, pp. 1431–1445, Feb. 2019.

[17] V. Monteiro, J. G. Pinto, and J. L. Afonso, "Experimental validation of a three-port integrated topology to interface electric vehicles and renewables with the electrical grid," *IEEE Trans. Ind. Inform.*, vol. 14, no. 6, pp. 2364–2374, Jun. 2018.
[18] A. Mondal, B. Nandan, D. Kastha, and P. Bajpai, "A three phase high power five-port current fed DC–DC converter for DC microgrid," in *Proc. IEEE Int. Conf. Power Electron., Drives Energy Syst. (PEDES)*, Piscataway, NJ, USA: IEEE Press, 2022, pp. 1–7.
[19] B. Liu, Y. Peng, J. Xu, C. Mao, D. Wang, and Q. Duan, "Design and implementation of multiport energy routers toward future energy internet," *IEEE Trans. Ind. Appl.*, vol. 57, no. 3, pp. 1945–1957, May/Jun. 2021.
[20] M. Jafari, Z. Malekjamshidi, D. D.-C. Lu, and J. Zhu, "Development of a fuzzy-logic-based energy management system for a multiport multioperation mode residential smart microgrid," *IEEE Trans. Power Electron.*, vol. 34, no. 4, pp. 3283–3301, Apr. 2019.
[21] R. T. Bambang et al., "Energy management of fuel cell/battery/supercapacitor hybrid power sources using model predictive control," *IEEE Trans. Ind. Inform.*, vol. 10, no. 4, pp. 1992–2002, Nov. 2014.
[22] F. Borrelli, A. Bemporad, and M. Morari, *Predictive Control for Linear and Hybrid Systems*. Cambridge, U.K.: Cambridge Uni. Press, 2017.
[23] T. Sasao, *Switching Theory for Logic Synthesis*. New York, NY, USA: Springer-Verlag, 2012.
[24] A. Schrijver, *Theory of Linear and Integer Programming*. Hoboken, NJ, USA: Wiley, 1998.
[25] A. Mallick, D. V. Tekumalla, A. R. Hota, and P. Bajpai, "Model predictive control based economic operation of grid-connected DC microgrid system," in *Proc. 9th IEEE Int. Conf. Power Syst. (ICPS)*, Piscataway, NJ, USA: IEEE Press, 2021, pp. 1–6.
[26] F. Garcia-Torres and C. Bordons, "Optimal economical schedule of hydrogen-based microgrids with hybrid storage using model predictive control," *IEEE Trans. Ind. Electron.*, vol. 62, no. 8, pp. 5195–5207, Aug. 2015.
[27] A. Chadly, E. Azar, M. Maalouf, and A. Mayyas, "Techno-economic analysis of energy storage systems using reversible fuel cells and rechargeable batteries in green buildings," *Energy*, vol. 247, 2022, Art. no. 123466.
[28] "Nedstack PEM fuel cell stacks," Nedstack Fuel Cell Stack Technology. Accessed: Jul. 30, 2024. [Online]. Available: https://nedstack.com/en/pem-fcs-stack-technology/pem-fuel-cell-stacks
[29] "48 volt modules—With dura blue technology," Maxwell Technologies. Accessed: Jul. 30, 2024. [Online].Available at https://maxwell.com/products/ultracapacitors/48v-module-with-durablue/
[30] S.-R. Moon and J.-S. Lai, "Multiphase isolated DC–DC converters for low-voltage high-power fuel cell applications," in *Proc. 22nd* Annu. IEEE Appl. Power Electron. Conf. Expo. (APEC), Piscataway, NJ, USA: IEEE Press, 2007, pp. 1010–1016.
[31] C. Liu, A. Johnson, and J.-S. Lai, "A novel three-phase high-power soft-switched DC/DC converter for low-voltage fuel cell applications," *IEEE Trans. Ind. Appl.*, vol. 41, no. 6, pp. 1691–1697, Nov./Dec. 2005.
[32] Y. Jang, M. M. Jovanovic, and Y. Panov, "Multiphase buck converters with extended duty cycle," in *Proc. 21st Annu. IEEE Appl. Power Electron. Conf. Expo. (APEC),* Piscataway, NJ, USA: IEEE Press, 2006, pp. 7–pp.
[33] C. Zhao, S. D. Round, and J. W. Kolar, "An isolated three-port bidirectional DC–DC converter with decoupled power flow management," *IEEE Trans. Power Electron.*, vol. 23, no. 5, pp. 2443–2453, Sep. 2008.
[34] W. Elmenreich and M. Delvai, "Time-triggered communication with UARTs," in *Proc. 4th IEEE Int. Workshop Factory Commun. Syst.*, Piscataway, NJ, USA: IEEE Press, 2002, pp. 97–104.
[35] R. W. Erickson and D. Maksimovic, *Fundamentals of Power Electronics*. New York, NY, USA: Springer-Verlag, 2007.
[36] C. Li, J. Liu, S. Du, N. Guo, Z. Deng, and H. Dang, "A current-fed dual-active-bridge integrated LC-resonant converter with dynamic power allocating for wide input and output voltage range operation," *IEEE Trans. Power Electron.*, vol. 39, no. 10, pp. 13413–13428, Oct. 2024.
[37] C. Madan, S. Kumari, and A. Halder, *Metal Oxides for Future Electrochemical Energy Storage Devices: Batteries and Supercapacitors*. Singapore: Springer Nature, 2023, pp. 291–330.

Arghya Mallick (Student Member, IEEE) received the B.Tech. degree from Jalpaiguri Government Engineering College, Jalpaiguri, West Bengal, India, in 2019, and the M.S. (by research) degree from the Indian Institute of Technology (IIT) Kharagpur, Kharagpur, West Bengal, India, in 2023, both in electrical engineering. He is currently working toward the Ph.D. degree in systems and control with Delft University of Technology, Delft, The Netherlands.

His research interests include decision-making under dynamic and uncertain environments.

Atanu Mondal (Student Member, IEEE) received the B.Tech. degree in electrical engineering from Maulana Abul Kalam Azad University of Technology, Kolkata, West Bengal, India, in 2018, and the M.Tech. degree in energy science and engineering in 2021 from the Indian Institute of Technology (IIT) Kharagpur, Kharagpur, West Bengal, India, where he is currently working toward the Ph.D. degree in specialization power electronics.

His research interests include topologies and control of dc–dc and ac–dc power electronics converters.

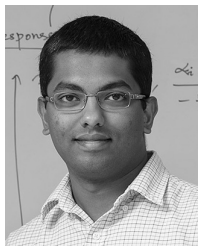

Ashish R. Hota (Senior Member, IEEE) received the B.Tech. and M.Tech. (dual degree) from the Indian Institute of Technology (IIT) Kharagpur, Kharagpur, India, in 2012, and the Ph.D. degree from Purdue University, West Lafayette, USA, in 2017, all in electrical engineering.

He is an Assistant Professor with the Department of Electrical Engineering, IIT Kharagpur, and a Young Associate with the Indian National Academy of Engineering (INAE). His research interests include in the areas of game theory, stochastic optimization, and control of network systems.

Debaprasad Kastha (Senior Member, IEEE) received the Ph.D. degree in electrical engineering (specialization: machine drives) from the University of Tennessee, Knoxville, TN, USA, in 1993.

In 1994, he joined the Department of Electrical Engineering, Indian Institute of Technology (IIT) Kharagpur, Kharagpur, India, where he became a Professor in 2011. He has been teaching and doing research in the area of power electronics and drives for more than two decades and has authored or co-authored about 50 technical papers, books, and electronic teaching aids. His research interests include the areas of wind power generation, machine drives, dc power supply, and distribution systems.

Prabodh Bajpai (Senior Member, IEEE) has received the B.E. degree in electrical engineering from the Indian Institute of Technology (IIT) Roorkee, Roorkee, India, the M.Tech. degree in energy studies from IIT Delhi, New Delhi, India, and the Ph.D. degree in electrical engineering from IIT Kanpur, Kanpur, India.

Currently, he is working as a Professor with the Department of Sustainable Energy Engineering, IIT Kanpur. His research interests include renewable energy systems, smart grid, solar PV microgrids, and power system restructuring.